The Astronomical Journal, 159:152 (14pp), 2020 April https://doi.org/10.3847/1538-3881/ab7334

MUSE Observations of NGC330 in the Small Magellanic Cloud: Helium Abundance of Bright Main-sequence Stars*

R. Carini[1], K. Biazzo[2,1], E. Brocato[1,4], L. Pulone[1], and L. Pasquini[3]
[1] INAF—Osservatorio Astronomico di Roma, via Frascati 33, I-00078 Monte Porzio Catone, Italy; roberta.carini@inaf.it
[2] INAF—Osservatorio Astrofisico di Catania, via S. Sofia 78, I-95123 Catania, Italy
[3] ESO—European Southern Observatory, Karl Schwarzchild Str. 2, Garching b. Munchen, Germany
[4] INAF—Osservatorio Astronomico d'Abruzzo, Via M. Maggini snc, I-64100 Teramo, Italy
Received 2019 June 14; revised 2020 January 31; accepted 2020 February 3; published 2020 March 13

Abstract

We present observations of the most bright main-sequence stars in the Small Magellanic Cloud stellar cluster NGC 330 obtained with the integral-field spectrograph, the Multi Unit Spectroscopic Explorer, at the Very Large Telescope. The use of this valuable instrument allows us to study both photometric and spectroscopic properties of stellar populations of this young star cluster. The photometric data provide us a precise color–magnitude diagram, which seems to support the presence of two stellar populations of ages of ≈18 Myr and ≈30 Myr assuming a metallicity of $Z = 0.002$. Thanks to the spectroscopic data, we derive a helium abundance of 10 main-sequence stars within the effective radius of $R_{\rm eff} = 20''$ of NGC 330, thus leading to an estimation of $\langle \epsilon\,({\rm He})\rangle = 10.93 \pm 0.05(1\sigma)$. The helium elemental abundances of stars likely belonging to the two possible stellar populations do not show differences or dichotomy within the uncertainties. Thus, our results suggest that the two stellar populations of NGC 330, if they exist, share similar original He abundances. If we consider stellar rotation velocity in our analysis, a coeval (30 Myr) stellar population, experiencing different values of rotation, cannot be excluded. In this case, the mean helium abundance $\langle \epsilon\,({\rm He})\rangle_{\rm rot}$ obtained in our analysis is 11.00 ± 0.05 dex. We also verified that possible non-LTE (NLTE) effects cannot be identified with our analysis because of the spectral resolution and they are within our derived abundance He uncertainties. Moreover, the analysis of the He abundance as a function of the distance from the cluster center of the observed stars does not show any correlation.

Unified Astronomy Thesaurus concepts: Stellar abundances (1577); Small Magellanic Cloud (1468); Star clusters (1567)

1. Introduction

NGC 330 has been early recognized as one of the most populated (total mass of ~ 3.6–$3.8 \times 10^4\,M_\odot$; Mackey & Gilmore 2003; McLaughlin & van der Marel 2005) and brightest young stellar cluster (∼30 Myr; e.g., Sirianni et al. 2002; Keller et al. 2000) of the Small Magellanic Cloud (SMC; Arp 1959; Robertson 1974). The color–magnitude diagram (CMD) of the cluster discloses a blue main sequence and two clumps of supergiant stars, located in the red and blue part of the diagram, clearly recognizable and distinct from the main-sequence stars. These features can be understood in terms of massive stars experiencing the core H-burning phase (main sequence) and the core He-burning phase (clumps). Moreover, the presence of a quite high fraction of Be stars is also well established (Feast 1991), which makes the interpretation of this cluster complicated and, at the same time, challenging (e.g., Grebel & Richtler 1992; Caloi et al. 1993; Grebel et al. 1996; Keller et al. 1999, 2000; Martayan et al. 2007a, 2007b; Tanabé et al. 2013). Nevertheless, NGC 330 remains a very attractive laboratory to improve our knowledge about the stellar evolution theory and the physics of intermediate mass stars born in a low-metallicity environment such as the SMC. For instance, from an evolutionary point of view, the ratio between the number of blue and red supergiants represents a fair indicator of the relative time an intermediate mass star spends along the He-burning loop. The quoted large fraction of Be stars (∼60%) allows us to investigate the role of rotation in intermediate mass stars (Grebel & Richtler 1992; Grebel et al. 1996; Lennon et al. 1996; Mazzali et al. 1996; Keller & Bessell 1998; Keller et al. 1999; Maeder et al. 1999; Lennon et al. 2003). Moreover, NGC 330 represents an interesting cluster to investigate the possible presence of multiple populations in a young, metal-poor environment like the SMC. Multiple stellar populations are found in the literature in Galactic Globular Clusters (GGCs; e.g., Piotto 2010; Gratton et al. 2012, 2019, and reference therein). These latter systems are characterized by two (or more) groups of stars, one with the same chemical abundance of halo stars, usually referred to as primordial or first population (FG), and the other (the second generation, SG) enriched in He, N, Na, Al, and poor in O and Mg with respect the FG stars (e.g., Carretta et al. 2009; Carretta 2015; Carretta et al. 2018). In particular, the enhancement of the He abundance explains the peculiarities in the CMDs of these systems, as the main-sequence split and the blue tails of the horizontal branch. The difference in helium between the populations can be as high as ∼0.1–0.2 dex in He mass fraction Y (e.g., D'Antona & Caloi 2004; Piotto 2008; Pasquini et al. 2011). This is confirmed by Marino et al. (2014) who provided the first direct spectroscopic measurement of highly He-enhanced ($Y \sim 0.34$) SG stars in the blue horizontal branch of the globular cluster NGC 2808. The new paradigm for the interpretation of these observations is that the GGCs are composed by two (or more) populations of stars; the SG stars were born from matter expelled by evolving stars of the FG

* Based on observations made with the MUSE integral-field spectrograph operating at the Very Large Telescope (Sierro Paranal, Chile) during the commissioning of the instrument.

stars and nuclearly processed through the hot CNO cycle. According to the theoretical scenarios that try to explain the phenomena of the multiple populations in Globular Clusters (GCs), the process of formation of the SG stars happened within 100–150 Myr from the formation of the FG stars (Decressin et al. 2007; D'Ercole et al. 2008, 2016; Bastian et al. 2013; Gieles et al. 2018).

In the recent years, the presence of multiple populations in Magellanic Cloud (MC) GCs, similar to those found in the Milky Way, has been demonstrated by observational evidences. It was indeed found that many star clusters in the MCs show bimodal or extended main-sequence turnoff (eMSTO) and dual clump in their CMDs, suggesting the presence of the multiple populations of stars with possible different ages (e.g., Mackey & Broby Nielsen 2007; Glatt et al. 2008; Girardi et al. 2009; Milone et al. 2009; Goudfrooij et al. 2014). More recently, in young stellar clusters (age less than 600 Myr) have been observed not only in the eMSTO, but also in the split of the main sequence, similar to that detected in Milky Way GCs (Milone et al. 2015, 2016, 2017, 2018). These photometric evidences could be interpreted with the presence of stellar populations with different ages, but also with coeval populations with different stellar rotation velocity (e.g., Bastian & de Mink 2009; Brandt & Huang 2015; D'Antona et al. 2015; Marino et al. 2018). Until now, spectroscopic studies of stars in MC clusters younger than ∼2 Gyr do not show differences in light elements between stellar populations of young massive clusters (Mucciarelli et al. 2014; Martocchia et al. 2017), contrary to what is observed in the GGCs. Only recently, Lagioia et al. (2019b) have found traces of He enhancement ($\Delta Y \sim 0.010 \pm 0.006$ dex) in the second population of stars of four ∼6–10 Gyr extragalactic GCs (NGC 121, NGC 339, and NGC 416) within the SMC. This has been confirmed by the analysis of Chantereau et al. (2019). Moreover, in stars of GCs in the MCs with an age between 2 and 10 Gyr, differences in the nitrogen abundance have been observed (Lagioia et al. 2019a).

From these evidences, it is not clear if the young massive stellar clusters with multiple populations are the younger counterparts of the old GGCs. In this context, we started a project to investigate the stellar content and the He abundance of the stars populating the SMC young cluster NGC 330.

The presence of multiple populations in NGC 330 is supported by the analysis of Chiosi et al. (1995), who found for the cluster a spread in age of 10–25 Myr from classical semi-convective models, and 10–48 Myr from full and diffusive overshoot models. Li et al. (2017) found that the rotation alone is not able to explain the eMSTO of NGC 330. They also pointed out that an age spread of 35–50 Myr can help in minimizing the problem. Instead, Bodensteiner et al. (2020) found an age between 35 and 40 Myr. So the presence and/or the origin of the age spread remains still unknown.

The Multi Unit Spectroscopic Explorer (MUSE; Bacon et al. 2010) operating at the Very Large Telescope (VLT) of the European Southern Observatory (ESO) provided us with the opportunity to obtaining simultaneously photometric and spectroscopic data for a large number of stars in NGC 330. Thanks to the exceptional observing capabilities of this instrument, in this work we investigate the presence of multiple populations and possible star-by-star differences in helium abundance.

Table 1
Selected Parameters of MUSE in a Nutshell and Relevant Quantities of the Observations

Parameter	Value
Number of IFU models	24 (images slicer + spectrograph + CCD)
Wavelength coverage	4800–9300 Å (nominal range)
Field of view	$59'' \times 60''$ (WFM)
Spatial sampling	$0''.2$ (WFM)
Multiplex factors	1152 slices, 90000 spaxels, 3700 wavelength bins
R.A. (J2000)	00:56:18.2
Decl. (J2000)	−72:27:47.8
Mean seeing	$1''.3$
Airmass	$1''.5$
T_{exp}	200 s
Mean spectral resolution	2.75 Å

In the present paper, we describe the observations and data reduction in Section 2, while the analysis of the photometric data are presented in Section 3, together with the comparison to isochrones of different ages and rotation velocity to obtain hints on the presence of multi-populations. The spectroscopic data analysis and the measurement of He abundances are presented in Section 4. The effect of stellar rotation is also considered in this section. The discussion on the age of the cluster and on the radial distribution of He abundances are reported in Section 5, while the final remarks are provided in Section 6.

2. Observations and Data Reduction

NGC 330 was observed with the integral-field spectrograph MUSE (Kelz et al. 2016) operating at the VLT during the commissioning run on 2014 August 3. The observation covered the central area of NGC 330, with a field of view of $\sim 1 \times 1$ arcmin^2, a pixel scale of $0''.20$ pixel^{-1}, and a total exposure time of 200 s. For this observation the normal wide-field mode was used and the parameters of the instrument setup adopted are summarized in Table 1.

The data reduction of the instrumental raw data from the 24 CCDs was performed using the MUSE pipeline (Weilbacher et al. 2014). This procedure provides a reduced datacube (two spatial and one wavelength axis) where bias subtraction, flat fielding, and flux and wavelength calibration are properly taken into account. Correction for instrumental and atmospheric effects, geometrical calibration, and sky subtraction are also performed within the context of this pipeline. As a result of this data reduction procedure, Figure 1 shows the image of NGC 330 at ∼4800 Å.

The region of NGC 330 covered by our MUSE observations is comparable with the annulus "A" of Robertson (1974) and allows us to analyze a sample of stars in the very center of the cluster, where the field contamination is low and most of the stars are members. On the other side this implies that the effect of crowding in NGC 330 should be evaluated. Since we intend to derive a CMD of the brightest stars populating NGC 330, two broadband images (using the V and I passbands as defined by Landolt 1992) were extracted from the datacube. In this way, we were able to derive the photometry and CMD directly from our data.

Moreover, we extracted from MUSE database the spectra of a sample of 10 B stars (Figure 2). In particular, we selected one

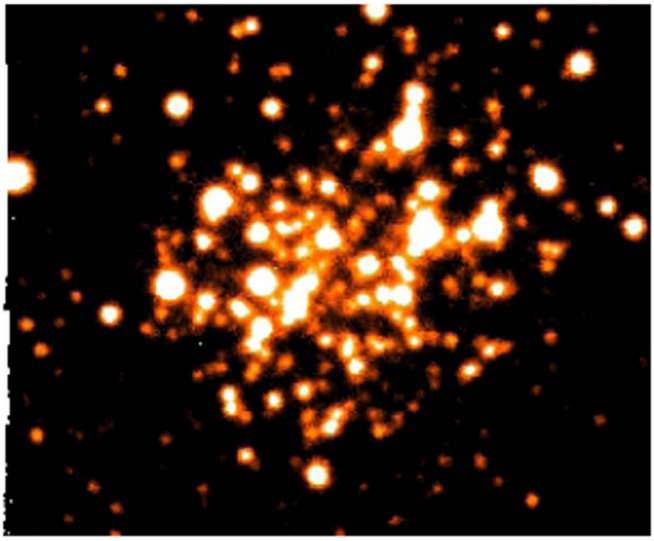

Figure 1. MUSE image of NGC330 at $\lambda \sim 4800$ Å. North is up and east is to the left.

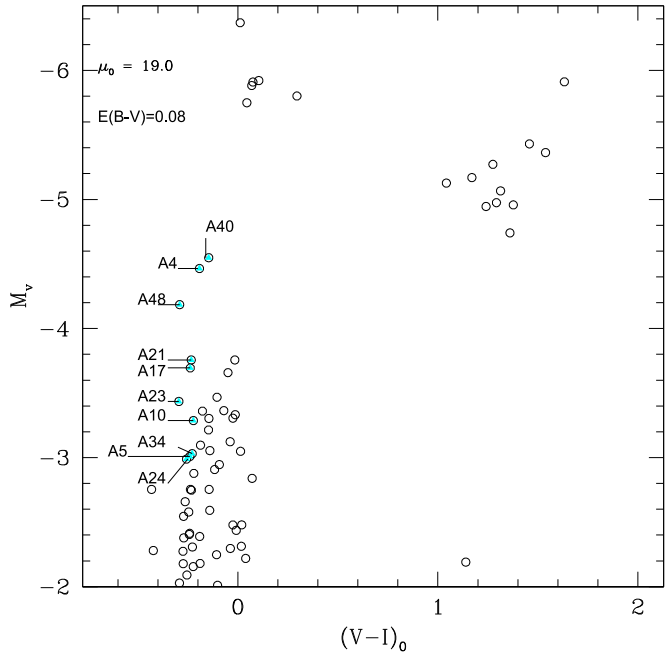

Figure 2. Observed CMD of NGC 330. The name of the stars (designation from Robertson 1974) analyzed in this work are also reported.

by one the stars suffering less severe crowding and, in case of moderate overlapping point-spread functions (PSFs), we took particular care in extracting the spectra from the central region of the PSF where the flux of a nearby star was negligible. Clearly, this implies a slightly lower signal-to-noise (S/N) for the selected star but minimizes the contamination of the nearby star in the extracted spectra. Taking advantage of the PSF analysis performed with *daophot* (Stetson 1987), we obtained spectra that contain most of the flux of the PSF ($\geqslant$80%). Low values ($\sim$80%) are due to the safe selection we adopted in avoiding the contamination from nearby stars. Therefore, we expect a negligible impact of crowding on the spectrum extraction. The whole spectrum of one of the selected stars (namely, A17) is shown in Figure 3 where the typical steepness and features of B stars can be recognized.

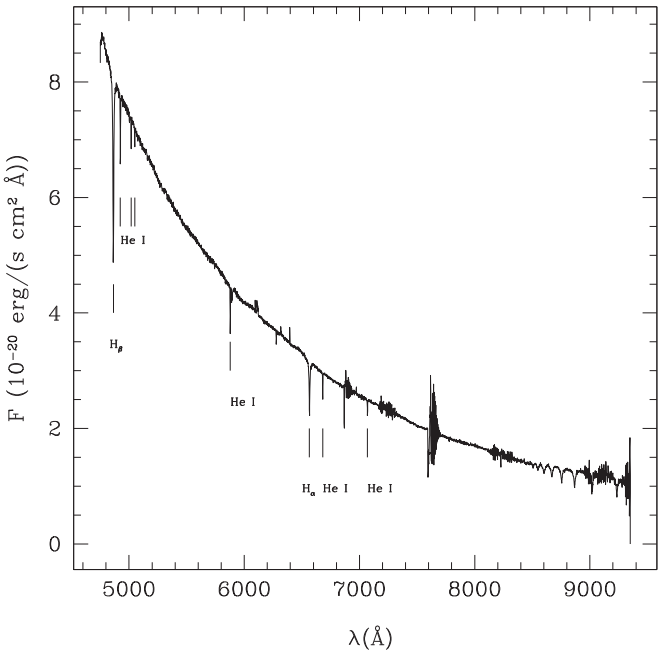

Figure 3. The entire spectrum of the B star A17 in NGC 330 obtained with MUSE at the VLT.

The spectra were also corrected for atmospheric absorption features. We used the software Molecfit, a tool distributed by the ESO and based on synthetic transmission spectra calculated by a radiative transfer code (Kausch et al. 2015; Smette et al. 2015). Molecfit models the most appropriate atmospheric profile (i.e., the variation in temperature, pressure, and humidity as a function of the altitude) at the time of the given science observations. As input it requires ambient parameters (e.g., telescope altitude angle, humidity, pressure, ambient temperature, mirror temperature, elevation, longitude, and latitude), instrumental parameters (e.g., slit width, pixel scale), molecular columns (i.e., which molecules have to be considered, which depend on the spectral region analyzed), background and continuum (e.g., flux unit, polynomial fit for continuum), spectroscopic resolution, and so on. In the wavelength range of MUSE the relevant molecules are O_2 and H_2O. A single atmospheric profile is compiled from data from three sources: a standard atmospheric profile for a given climate zone (produced for the Michelson Interferometer for Passive Atmospheric Sounding on board the ENVISAT satellite), Global Data Assimilation System model profile, and the corresponding ground-based by the ESO Meteo Monitor measurements. The first one includes information on pressure, temperature, and molecular abundances as a function of height. The second one is provided by the National Oceanic and Atmospheric Administration (NOAA),[5] which gives information about the weather forecast for the location of Cerro Paranal to an altitude of $\sim$26 km. The third one provides information on the local meteorological conditions in the ESO site Paranal taken from a local meteo station mounted 30 m high. After several iterations of the χ^2 minimization procedure, Molecfit writes the best-fit spectrum for telluric correction. This process takes into account the optimization for scaling the wavelength grid and the resolution of the model. On the basis of this fit, the code calculates the atmospheric transmission for

[5] http://140.90.198.158/pub/gdas/rotating

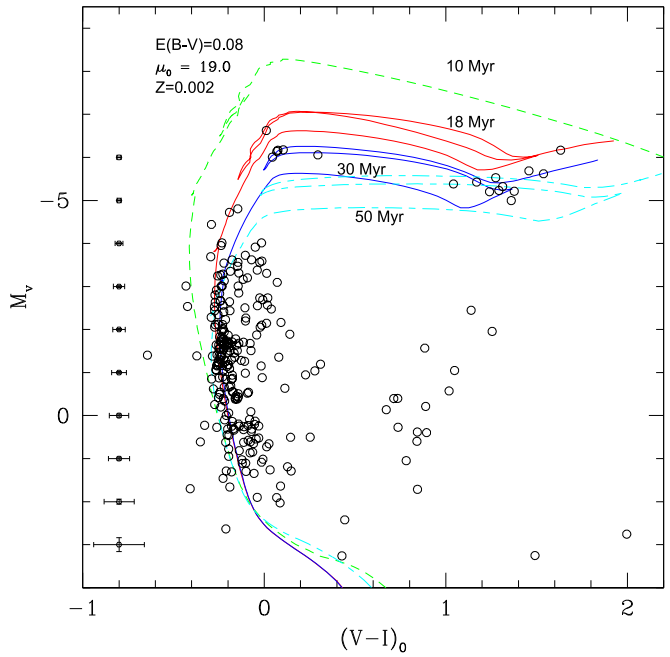

Figure 4. Color–magnitude diagram of the selected stars in NGC 330. The isochrones at 10, 18, 30, and 50 Myr obtained from PARSEC (Bressan et al. 2012; Marigo et al. 2017) are overplotted with short green dashed, red solid, blue solid, and cyan short–long lines, respectively. The best-fitting isochrones are 18 Myr and 30 Myr.

the wavelength range of the input spectrum and corrects it for telluric absorption. We applied this procedure for each spectrum.

3. Photometry and Comparison with Isochrones

The V and I images have been analyzed using the *daophot* package developed to perform stellar photometry in crowded fields (Stetson 1987). The detection threshold to 5σ above the background level was adopted. We selected a dozen of stars external to the core of the cluster to find the best PSF. Instrumental v and i magnitudes were converted into the standard V and I Johnson/Cousins system using, as calibrators, 12 stars in the MUSE field already detected and with magnitudes measured by Udalski et al. (1998, 2008).[6] The resulting adopted calibration equations are

$$V = v - [0.009 \pm 0.009](v - i) + [3.814 \pm 0.008]$$
$$I = i + [0.009 \pm 0.009](v - i) + [2.526 \pm 0.009].$$

The uncertainties in the coefficients are the formal errors in the linear regression. The range in colors of the Udalski reference stars used as calibrators is inside the interval $-0.14 < V{-}I < 1.61$. The color coverage of the adopted standards is totally adequate at the blue and red extremes, leaving slightly outside only a couple of red giants.

As a final result of the analysis performed with *daophot*, the V and I photometry of about 250 bright stars with a mean uncertainty of $\sim$0.01 mag was obtained. In this sample, 34 stars are found in common with Robertson (1974) and in the following they will be indicated with the same name (i.e., with the prefix A). In Figure 4 the CMD obtained with our measures is presented by assuming a distance modulus μ_0 of 19.0 mag and a reddening of $E(B-\mathrm{V}) = 0.08$ mag (see Caloi et al. 1993; Keller et al. 2000). In the same figure, we also overplot the PAdova and TRieste Stellar Evolution Code[7] (PARSEC; Bressan et al. 2012; Marigo et al. 2017) isochrones with $Z = 0.002$ (Reitermann et al. 1990; Spite et al. 1991) and without rotation.

The quite broad main sequence extends up to $M_V \sim -4.5$ mag ($m_V = 14.5$ mag), in agreement with Chiosi et al. (1995) and Li et al. (2017; see also reference therein), where the red and the blue groups are also clearly represented in our sample. These blue and red groups of stars, which are quite brighter than the main-sequence termination, seem to be core He-burning stars populating the hot and cool limit of the well-known loop of the effective temperature foreseen for stellar models of intermediate mass ($\approx$3–10 $M_\odot$) stars. The loop extends from $(V{-}I)_0 \approx 0.0$ mag up to $\approx$1.5 mag. The extended main-sequence turnoff has been already extensively discussed in Chiosi et al. (1995) and especially in Li et al. (2017) and we confirm here the difficulty of interpreting this feature of the CMD of NGC 330. Nevertheless, we note that the two isochrones of 18 and 30 Myr overlap fairly well the position of the main-sequence stars. More interestingly, the two extended loops of the isochrones, which are due to stars experiencing the core He-burning phase, appear to reproduce quite precisely the luminosities and the colors of the blue and red groups of supergiants. It is relevant to recall that stellar models of intermediate mass (of the adopted metallicity) predict that the evolutionary time of the He-burning phases is spent part at low $T_{\rm eff}$ ($\leqslant$4000 K) and part at very high $T_{\rm eff}$ ($\geqslant$12,000 K; Stothers & Chin 1992; Brocato & Castellani 1993; Chiosi et al. 1995; Langer & Maeder 1995; Marigo et al. 2017).

It should be noted that the blue supergiant group is composed of one very bright and hot star ($V \sim -6.5$ mag and $(V{-}I)_0 \sim 0.0$ mag) just overlapping the blue part of the He-burning loop of the 18 Myr old isochrone. A subgroup of four stars are $\approx$0.5 mag fainter than this star and overlap perfectly the bluest part of the He-burning loop of the 30 Myr old isochrone.

The CMD seems to suggest that also the blue supergiants show a spread/separation in magnitude and colors. If these precise overlaps of He-burning loops are considered real features of the NGC 330 stellar population, we find that two isochrones separated by $\simeq$12 Myr are able to reproduce the data adopting reasonable distance, reddening, and metallicity values. This result is compatible with the findings of Li et al. (2017). In order to provide a quantitative example of how the isochrones change if different ages are assumed, we plot in Figure 4 two isochrones with 10 Myr and 50 Myr. The figure shows that the isochrone with 10 Myr does not match the location of the observed stars, while the 50 Myr one reproduces the main-sequence stars but the coolest (and more populated) part of the core He-burning phase is much redder than the location of the red clump stars. We stress here that our outcome is based on very few supergiants and needs further confirmation. Nevertheless, one single isochrone is not able to fit all the supergiants of NGC 330 and at least two isochrones are required to fit the stars in the He-burning phase due to the observed spread/separation in their magnitudes ($\Delta V \simeq 0.5$ mag). In fact, it is quite unlikely that these supergiant stars ($m_V \leqslant 14.0$ mag) have differential uncertainties

[6] http://ogledb.astrouw.edu.pl/~ogle/photdb/index.html

[7] http://pleiadi.pd.astro.it/

of the order of $\Delta M_V \simeq 0.5$ mag, which should be needed to reconcile the observed magnitude to one single isochrone.

Finally, we have to recall that the presence of binaries cannot be excluded. This occurrence could also explain the location of the brightest stars in the CMD that we address as the youngest population. We suggest here that higher resolution spectroscopy of these stars is required to provide conclusive results on this issue.

3.1. Effect of Stellar Rotation

We dedicate a paragraph to the discussion on stellar rotation, because, even if our spectra do not have the resolution high enough to analyze this issue in detail, it is known that many OB stars are fast rotators (v sin i up to 300 km s^{-1}). In particular, Hunter et al. (2011), analyzing high-resolution VLT Fibre Large Array Multi Element Spectrograph (FLAMES) data for stars in the Large Magellanic Cloud (LMC) and SMC, found that the mean v sin i for 77 B-type stars of NGC 330 with masses less than 25 $M_\odot$ (as in our sample) is about 150 km s^{-1}. Stellar rotation is a parameter directly related to the size of the convective core (for a detailed treatment of the rotation we quote, e.g., Maeder & Meynet 2000; Meynet & Maeder 2000 and references therein). Here, we recall only the main effects of the rotation on the evolution of the B stars at low metallicity:

1. the convective core of the stars increases during the MS phase;
2. the luminosity of a rotating star is higher (about 0.5 mag) than that of a non-rotating star of the same mass;
3. the combination of these two effects implicates that the lifetime in the H-burning phase grows, but only moderately (about 20%–30% for an initial velocity of 200 km s^{-1});
4. the envelopes of rotating stars (angular velocity $\omega > 0.5$ ω_c, with ω_c as the critical angular velocity) are enriched in CNO-processed material, in particular of He and N for stars with $M > 10M_\odot$;
5. also during the He-burning phase the luminosity is higher because of the larger He cores, if the mass loss is not too strong;
6. and the rotation inhibits the formation of stars in the red clump during the He-burning phase, but this is contrasted by the mass-loss effect that favors the formation of red supergiants. Until now the models could not reproduce the ratio between blue and red supergiants in the solar neighborhood observed at the metallicity of the SMC (Brunish et al. 1986; Schaller et al. 1992). Some models for the most rapid rotators at low metallicity predict the disappearance of the red clump, and the He-burning occurs only in the blue part of the HR diagram (log $T_{\rm eff} \sim 4$; Georgy et al. 2014).

We have compared our CMD, which includes also the core He-burning loop, with isochrones of rotating models from the Geneva stellar model database[8] (Georgy et al. 2014), provided by the SYCLIST code. We took into account the work done by Milone et al. (2018), in which they show the presence of two families of stars in NGC 330, the bluest formed by non-rotating stars with an age compatible with 32 Myr (in agreement with our results) and the reddest by rotating stars with an angular velocity of $\omega = 0.9\omega_c$ and age around 40 Myr, representing 40%–55% of main-sequence stars.

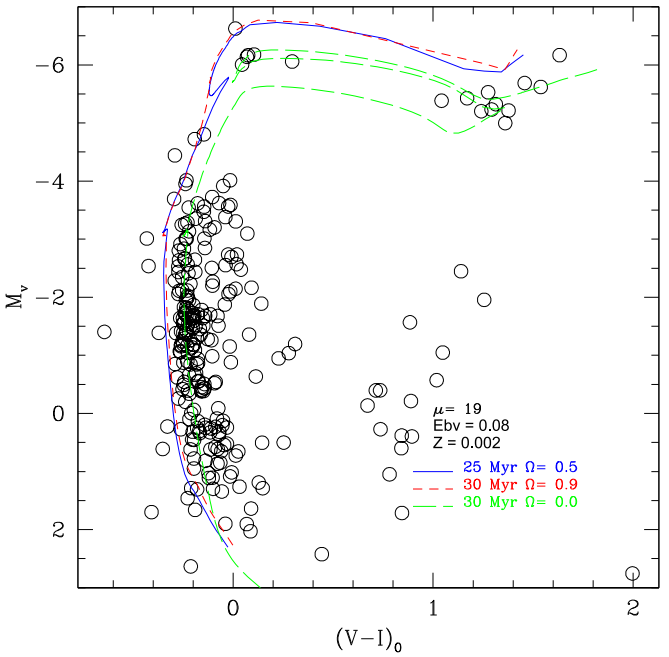

Figure 5. Color–magnitude diagram of NGC 330. The isochrone at 30 Myr is obtained from PARSEC (Bressan et al. 2012; Marigo et al. 2017; the green long dashed line); the isochrones computed from rotating stellar models at 25 Myr with $\omega = 0.5\omega_c$ (blue line) and at 30 Myr with $\omega = 0.9\omega_c$ (red dashed line) are taken from Georgy et al. (2014). The adopted values for the age, distance modulus, reddening, and metallicity are quoted in the figure.

As shown in Figure 5, it is evident that the evolutionary track of Geneva predicts the absence of the red clump with this age and rotation, so they cannot explain the majority of the He-burning stars. For this reason, the presence of two populations is required. One composed by non-rotating 30 Myr old stars (green long dashed line) The second one can be identified by the stars superimposed to the isochrones of rotating models at 25 Myr with $\omega = 0.5$ ω_c (blue line) and 30 Myr with the $\omega = 0.9$ ω_c (red dashed line).

In this case, we remain with a (nearly) coeval population formed by a mixture of rotating and non-rotating stars. We keep in mind that the claim that the cluster includes a secondary rotating population is based on the location of one blue giant star, like the previous scenario where a 18 Myr population has been suggested (see Figure 4). The presence of stars with $-5.5 < M_v < -4$ mag, after the overall contraction, could favor the isochrone with $\omega = 0.9\omega_c$ because they should be He-burning stars. One of these stars is A4, already analyzed by Lennon et al. (2003) who found v sini $= 20$ km s^{-1}, thus favoring the hypothesis that the second family of stars are not fast rotators. We remark here that the overshooting is stronger in the Padova evolutionary tracks with respect to the Geneva ones, so an error of about 5 Myr should be also taken into account.

4. Spectra Extraction and Analysis

In this section, we make use of the spectral data secured by MUSE observations to investigate the presence of a possible spread of helium abundances in the B stars of NGC 330. Such a difference would be extremely interesting because it would support the possible existence of two or more populations with

[8] https://www.unige.ch/sciences/astro/evolution/en/database/syclist/

Table 2
Input (Photometric) and Output (Spectroscopic) Parameters Obtained from Our Analysis

Star	$T_{\rm eff}^{\rm phot}$(K)	$\sigma(T_{\rm eff}^{\rm phot})$(K)	$\log g^{\rm phot}$	$\sigma(\log g^{\rm phot})$	$T_{\rm eff}^{\rm spec}$ (K)	$\sigma(T_{\rm eff}^{\rm spec})$(K)	$\log g^{\rm spec}$	$\sigma(\log g^{\rm spec})$	$V_{\rm rad}$(km s^{-1})	$\sigma(V_{\rm rad})$ (km s^{-1})	S/N
A4	20000	1000	3.0	0.5	17000	1000	2.7	0.1	152	8	300
A5	24000	1000	4.0	0.5	22500	2000	3.7	0.2	155	40	100
A10	22000	1000	4.0	0.5	22500	1000	3.9	0.1	140	20	130
A17	24000	1000	4.0	0.5	22000	1000	3.7	0.1	147	15	200
A21	23000	2000	4.0	0.5	23500	1500	3.9	0.2	150	20	200
A23	33000	2000	4.0	0.5	22000	1000	3.6	0.2	142	11	200
A24	26000	2000	4.0	0.5	23000	3000	4.1	0.4	140	25	100
A34	23000	1000	4.0	0.5	22500	2000	4.0	0.2	145	20	120
A40	16000	1000	3.0	0.5	18500	500	3.2	0.1	145	10	300
A48	32000	2000	4.0	0.5	25000	2500	3.6	0.5	152	45	200

Note. Errors in spectroscopic parameters are listed for each target. Typical S/N at about 6000 Å are reported in the last column.

different He content, and would also help in alleviating the tension between models and the extended MSTO observed in NGC 330 (Li et al. 2017). Furthermore, He is a key element in the context of the multiple populations in globular clusters (D'Antona & Caloi 2004; Piotto et al. 2007; Piotto 2008) and discovering the presence of dichotomy or spread of He abundance within star members of a young clusters like NGC 330 would be extremely interesting. The high temperatures of these B stars ensure the presence of He I features in their spectra. We decided to exclude Be stars to minimize uncertainties due to rotation and complexity in the spectra analysis.

4.1. Spectroscopic Stellar Parameters

The procedure adopted to derive the He abundances from the spectra of the selected B stars is briefly outlined in this section.

We used the Spectroscopy Made Easy[9] (SME, version 522; Valenti & Piskunov 1996; Piskunov & Valenti 2017) package to determine the fundamental parameters (effective temperature $T_{\rm eff}$, surface gravity $\log g$, radial velocity $V_{\rm rad}$) and He abundance. The measurements of these quantities was performed in a few key steps and synthetic spectra were computed to obtain the best fit of the observed spectroscopic data. SME is a spectral synthesis code that allows us to find the best fit of an observed spectrum, assuming a wavelength range and initial input parameters. In particular, SME needs line list data for all atomic transitions of interest (i.e., element, ionization state, wavelength, excitation energy of the initial state, log gf; Vienna Atomic Line Database 3; Piskunov et al. 1995) and model atmospheres (ATLAS12; Kurucz 2013). Plane parallel geometry, negligible magnetic field, and no bulk flows are assumed by SME.

The parameter optimization code uses the Marquardt algorithm (Marquardt 1963; Press et al. 1992) to obtain estimates of the parameters, minimizing the χ^2 statistic by comparing model and observed spectra (Valenti & Piskunov 1996).

We assumed local thermodynamical equilibrium (LTE), as the resolution of the spectra is too low to appreciate the difference in He abundance due to non-LTE (NLTE). The evaluation of the effect of the NLTE on our results is treated in Section 4.4.

To derive stellar parameters removing the $\log T_{\rm eff} - \log g$ degeneracy, we decided to fit from normalized spectra the Hβ and the He I at 4921.9 Å features of each star considering the range 4800–5000 Å.

Before computing the synthetic spectra, input values of the stellar atmosphere have to be provided. To this purpose, we used both the photometric information obtained from our best isochrones fit and from the direct comparison with the colors of the Castelli & Kurucz (2003) models. The input values for each star of our sample can be found in Table 2 ($T_{\rm eff}^{\rm phot}$ and $\log g^{\rm phot}$). Moreover, we fixed the microturbulence at 5 km s^{-1}, which is a reliable value for B stars (see Lennon et al. 2003), and $Z = 0.002$ (i.e., [Fe/H] ~ -1; see Reitermann et al. 1990; Spite et al. 1991; Lennon et al. 1996, 2003; Hill 1999). The spectral resolving power ranges from ~1800 at 4800 Å to ~3600 at 9300 Å.

With these inputs, we determined $T_{\rm eff}$, $\log g$, and $V_{\rm rad}$ from the best fit of the spectra in the region Hβ-He I.

An example of the best fit of the Hβ and He I lines is shown in Figure 6 for the star A4.

The resulting stellar parameters ($T_{\rm eff}$, $\log g$, $V_{\rm rad}$) with their uncertainties, and the typical S/N at $\lambda \sim 6000$ Å, are reported in Table 2. We note that the reported values of the uncertainties obtained in the SME context, according with Press et al. (2002), refer to intrinsic errors, and they could be underestimated due to systematics, like reddening, theoretical assumption, etc.

4.2. Helium Abundance

Once the stellar parameters of each star were evaluated, we repeated the same steps as in the previous section but for the He features listed in Table 3, i.e., we considered the following wavelength ranges: 4880–4960 Å, 5000–5030 Å, 5030–5100 Å, 5860–5890 Å, 6640–6720 Å, and 7000–7100 Å (see Figures 7 and 8). As done for the determination of the stellar parameters, also for the He features we considered the atomic and molecular line list from VALD3 (Piskunov et al. 1995) and the spectra were normalized to their continuum level.

Stellar parameters were constrained to the values derived by fitting the Hβ and He I lines and then used to create the synthetic spectra around each He line. ATLAS12 model atmospheres (Kurucz 2013) were considered and the best fit was obtained around each spectral range through the SME package to derive the helium abundance. The values of the He abundance for each star and each feature are reported in Table 3. Internal errors computed by SME and mostly due to uncertainties in atomic parameters, stellar parameters, and

[9] Available at http://www.stsci.edu/~valenti/sme.html.

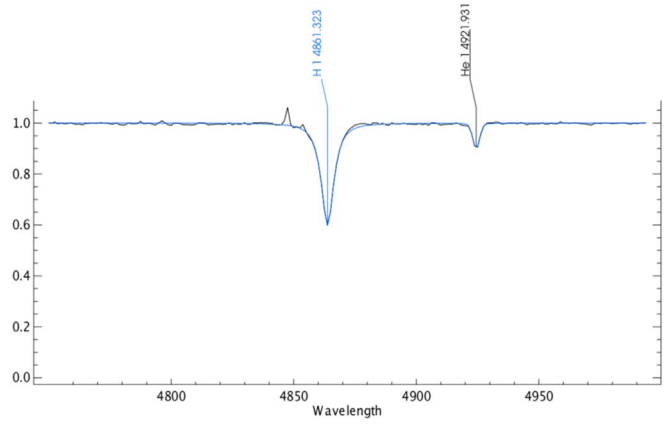

Figure 6. Best fit of the Hβ and He I lines (labeled) for the star A4.

continuum position are also reported. Empty values in this table refer to features for which the best fit was not obtained, in most cases because the observed line was too weak or not detectable. We also evaluated the impact of external errors considering the photometric $T_{\rm eff}$ and log g. To this aim we recomputed the best fit of each feature by adopting the photometric values of the stellar parameters and derived the mean errors in the final helium abundance of $\approx$0.1 dex and $\approx$0.05 dex due to the difference in the choice of $T_{\rm eff}$ and log g, respectively. These errors are indeed within the internal errors listed in Table 3. Systematic uncertainties could affect the helium abundance due to the effect of the assumption on the microturbulence. We tested the impact of varying the microturbulence from 0 to 10 km s^{-1}. The results show that an enhancement of microturbulence to 10 km s^{-1} leads to a decrease of He abundance of about 0.2 dex with respect the values determined with $\xi = 5$ km s^{-1}, while a value of $\xi = 0$ km s^{-1} leads to an increase of He up to 0.1 dex. The systematic uncertainties due to the debated value of metallicity in NGC 330 may affect the He determination. We calculated the He abundance of the stars in our sample by assuming the lowest ([Fe/H] $= -1.8$; Richtler & Nelles 1983) and the highest ([Fe/H] $= -0.5$; Meliani et al. 1995) values commonly assumed in the literature for this cluster. It turns out that the He abundance Y in our stars changes of an amount less than 0.01 dex.

In Figure 9 we show the logarithmic helium abundance (ϵ(He)[10] determined for each He I line (4921.9 Å, black circles; 5015.7 Å, red squares; 5047.7 Å, blue diamonds; 5875.6 Å, green stars; 6678.2 Å, magenta open triangles; 7065.7 Å, cyan filled triangles) and for each star analyzed. Uncertainties obtained by SME are also displayed.

We note that the He abundance determined for 6678.2 Å is systematically higher than the ones obtained from the other lines, except for the stars A5 and A48. This could be due to the contribution of the ^{3}He isotope enhancement (Schneider et al. 2018), which cannot be resolved in our spectra.

We then computed the mean of the He abundance values derived from the best fitted features for each star. This computation was afterwards repeated using only the values deviating less than 1σ from the initial average evaluation. This method allowed us to minimize the impact of single unpredictable errors provided by the best-fitting procedure of each He feature. The He abundances averages and the standard deviation σ of the average are reported in the eighth and ninth columns of Table 3, while the last column lists their corresponding helium mass fraction value (Y).

In order to check the reliability of our measurements, we also evaluated the weighted mean of the He abundances, i.e., using as weight the error on the ϵ(He) value obtained by fitting each single feature. As expected, we found that the two determinations of the He abundance are in full agreement within their internal uncertainties.

We notice that Lennon et al. (2003) have obtained spectra of a sample of seven stars in NGC 330 and one star (A4) is in common with our work. The $T_{\rm eff}$ and the surface gravity we derive in this work are in good agreement with the values obtained by these authors for the same star. However, the He abundance found by Lennon et al. (2003) using nine lines is ϵ(He) $= 10.66$, which is lower than the value found by us (i.e., ϵ(He) $= 10.94 \pm 0.22$).

In the following, we report the results of helium abundance for each B star analyzed in the present work.

A4

The spectrum of the star A4 presents one of the highest S/N ratios of our sample, with a value of about 300. The spectral regions where the He features used in this work are located are shown in Figure 7 (first solid lines from the top). The line 5015.7 Å is faint but the shape is regular and the best fit was obtained, even if the resulting He abundance for this feature is very low (ϵ(He) $= 10.35$). As already mentioned, this is the only star of our sample for which the He abundance has been reported by other authors (Lennon et al. 2003). They derived for this target spectroscopic values of $T_{\rm eff} = 18{,}000$ K, log $g = 2.8 \pm 0.2$, and microturbulence $\xi = 5$ km s^{-1}. These quantities are in very good agreement with our results ($T_{\rm eff} \sim 17{,}000 \pm 1000$ K, log $g = 2.7 \pm 0.1$) and with our choice to fix the microturbulence at the value of 5 km s^{-1} (see also Table 3).

However, we note that our mean value of the He abundance (ϵ(He) $= 10.94 \pm 0.22(1\sigma)$) is higher (more than 1$\sigma$) than the one found by Lennon et al. (2003), (ϵ(He)) $= 10.66$. We remark here that the abundance of this star is one of the lowest of the entire sample observed by Lennon et al. (2003).

A5

The S/N ratio of this star is about 100. The features at $\lambda = 5047.7$ Å, $\lambda = 5875.6$ Å, and $\lambda = 7065.7$ Å are noisy and hardly detectable, therefore no best fit was obtained. This star shows features larger than most of the other stars, thus suggesting very high rotation (see, in particular, the features centered at 5875.6 Å and 6678.2 Å). The mean value of the He abundance is ϵ(He) $= 10.93 \pm 0.01$.

A10

The effective temperature and the surface gravity derived from the synthetic spectra are in very good agreement with the photometric values (see Table 3). For the computation of the He abundance, we used all lines with the exception of the features at $\lambda = 5015.7$ Å and $\lambda = 5047.7$ Å. As found for A5, this star also shows very wide features, suggesting high rotation (see solid lines in the middle of each panel of Figure 7). In this case the derived He abundance resulted to be slightly subsolar

[10] ϵ(He) is defined to be $\log(N_{He}/N_H) + 12$, where $N_{\rm He}$ and N_H are the number densities of elements He and H, respectively.

Table 3
Helium Abundance (ϵ(He)) Derived from Our Analysis for Each Line

Star	ϵ(He) (λ4921.9 Å)	ϵ(He) (λ5015.7 Å)	ϵ(He) (λ5047.7 Å)	ϵ(He) (λ5875.6 Å)	ϵ(He) (λ6678.2 Å)	ϵ(He) (λ7065.7 Å)	$\langle\epsilon\,(\mathrm{He})\rangle$	σ	Y	σ(Y)
A4	10.94 ± 0.11	10.35 ± 0.05	10.93 ± 0.50	10.59 ± 0.02	11.10 ± 0.03	11.14 ± 0.45	10.94	0.20	0.26	0.18
A5	10.94 ± 0.30	10.93 ± 0.30	⋯	⋯	10.93 ± 0.89	⋯	10.93	0.01	0.25	0.01
A10	10.79 ± 0.27	⋯	⋯	10.9 ± 0.39	11.14 ± 0.71	10.78 ± 0.61	10.90	0.17	0.24	0.14
A17	10.89 ± 0.39	10.49 ± 0.13	10.96 ± 0.39	10.99 ± 0.32	11.32 ± 0.50	10.93 ± 0.15	10.94	0.04	0.26	0.04
A21	10.72 ± 0.26	10.62 ± 0.15	10.93 ± 0.54	10.93 ± 0.15	11.30 ± 0.34	11.01 ± 0.42	10.90	0.12	0.24	0.10
A23	10.95 ± 0.21	10.46 ± 0.37	10.94 ± 0.90	10.93 ± 0.24	11.61 ± 0.5	10.91 ± 0.25	10.93	0.02	0.25	0.02
A24	10.91 ± 0.44	⋯	10.95 ± 0.86	11.01 ± 0.37	11.53 ± 0.60	11.26 ± 0.47	11.03	0.16	0.30	0.15
A34	10.98 ± 0.37	10.93 ± 0.43	⋯	10.91 ± 0.30	11.23 ± 0.42	10.96 ± 0.32	10.95	0.03	0.26	0.03
A40	11.04 ± 0.08	10.85 ± 0.16	10.97 ± 0.07	10.88 ± 0.07	11.21 ± 0.05	10.83 ± 0.08	10.91	0.09	0.25	0.07
A48	10.54 ± 0.18	⋯	11.14 ± 0.14	10.93 ± 0.23	10.21 ± 0.20	10.75 ± 0.13	10.84	0.20	0.22	0.15

Note. Effective temperature and surface gravity are shown in Table 2.

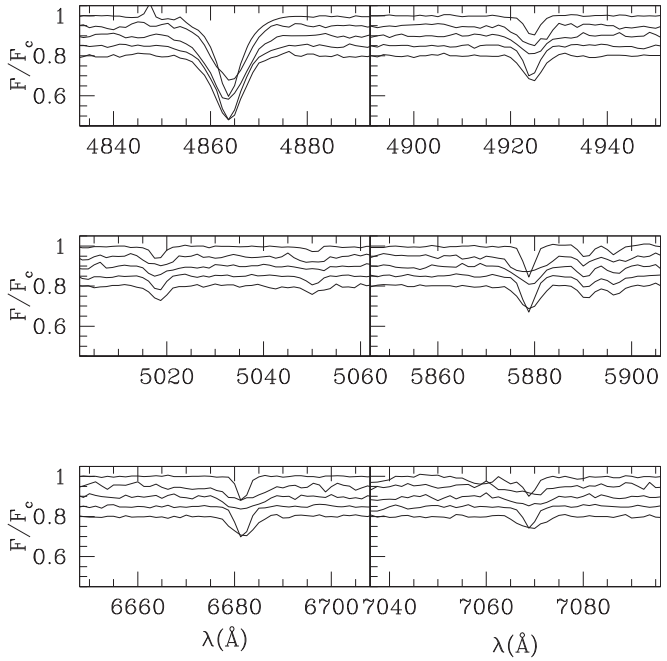

Figure 7. Each panel shows the region of the spectrum where the He features used in this work are located. The spectra are normalized but not redshifted. In every panel the spectra of the stars A4, A5, A10, A17, and A21 are plotted starting from the top and shifted of 0.05 in the y-axis for graphical reasons.

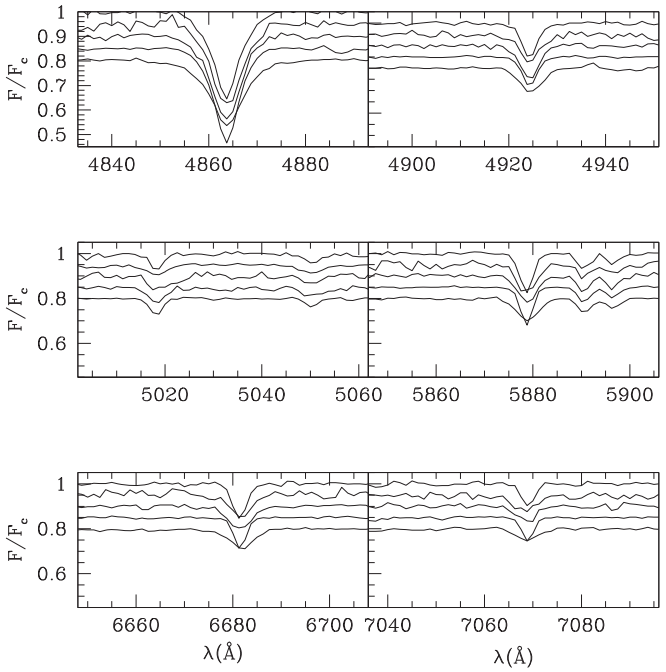

Figure 8. As for Figure 7, but for the stars A23, A24, A34, A40, and A48 (from top to bottom).

(i.e., 10.90 ± 0.17), if we assume $\epsilon(\mathrm{He})_{\odot} = 10.93$ as the helium solar abundance (Asplund et al. 2009).

A17

The effective temperature and the surface gravity are in agreement, within the uncertainties, with the theoretical values and all the selected He features were used to derive the final He abundance, which resulted as $\epsilon(\mathrm{He}) = 10.94 \pm 0.04$.

A21

Again the effective temperature and log g are in very good agreement with the photometric values. The lines are particularly broadened for this star, and the uncertainties in the determination of ϵ(He) is between 0.5 and 0.6 dex. The mean value is $\epsilon(\mathrm{He}) = 10.90 \pm 0.12$.

A23

From the photometry, we found that A23 is the target of our sample with the highest effective temperature (i.e., 33,000 K), while the result of the spectral best fitting of the Hβ and He I lines is very different (i.e., 22,000 K). Also in this case, all the He features were used for the calculation of the mean He abundance, resulting as solar.

A24

Spectroscopic effective temperature and surface gravity are in agreement, within the errors, with the theoretical values, despite the fact that the S/N ratio is one of the lowest within our sample (≈100). Almost each line could be considered to derive He abundance, with exception of λ5015.7 Å, with errors up to 0.4–0.5 dex. Accordingly, relative errors on effective temperatures are the largest one. The weighted average He abundance is 11.03 ± 0.16, the highest value of our sample. As for A5, the features are broadened, pointing out a possible high rotational velocity.

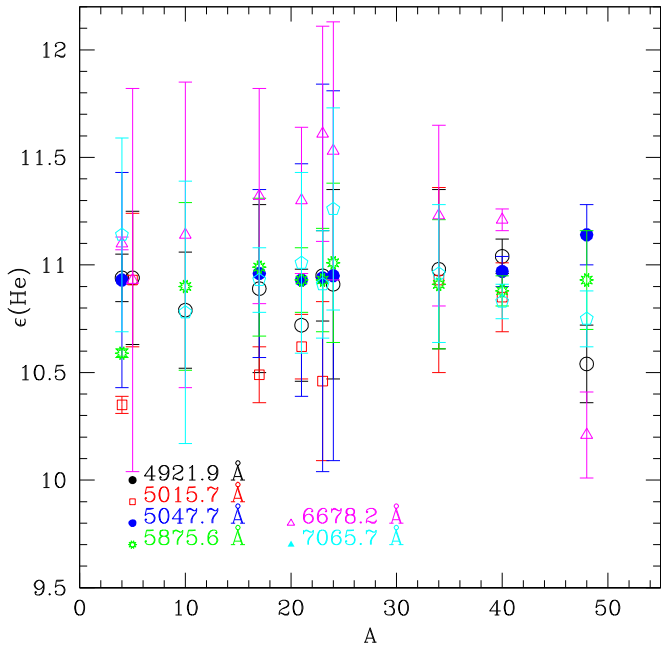

Figure 9. Logarithmic He abundance obtained for each helium line. Each symbol refers to a different line. Uncertainties obtained by SME are also shown. The *x*-axes reports the number of each star following the nomenclature by Robertson (1974).

A34

Also this star shows a relatively low S/N ratio (≈120) and consequently this leads to a poor determination of helium abundances from the single features, with uncertainties up to ∼0.5 dex. The final value of $\langle \epsilon\,(\mathrm{He})\rangle$ is indeed close to the solar value ($\epsilon(\mathrm{He}) = 10.95 \pm 0.03$; see Table 3).

A40

The S/N ratio of this star is very high, being larger than 350. The effective temperature from the spectra is slightly higher than the theoretical one, while the log *g* is in good agreement. All the He features were used to derive the He abundance; the He mean value is $\epsilon(\mathrm{He}) = 10.91 \pm 0.09$.

A48

Our spectroscopic best fit confirms the theoretical value of log *g* within the uncertainties, but not the $T_{\rm eff}$, which is lower of 7000 K. The lines of this target seem to suggest high $v \sin i$ (see Figure 8). We fitted each line except for λ5015.7 Å, $\epsilon(\mathrm{He}) = 10.84 \pm 0.22$.

4.3. Stellar Rotation

As already discussed in the previous sections, the stars in our sample could rotate and this may affect the spectral features. Unfortunately, the resolution of our spectra is too low to evaluate stellar rotation velocities lower than 150 km s^{-1}. We made an attempt to evaluate the contribution of the stellar rotation in the helium abundance. To this aim, we repeated the same procedure performed in Section 4.1 by adopting a rotating model framework. We first used the isochrone of 30 Myr with the angular velocity of $\omega = 0.9\omega_c$, already shown in Figure 5 to evaluate the input parameters ($T_{\rm eff}^{\rm phot}$, log $g^{\rm phot}$, $v \sin i$) for each star. These values are then used to compute the best fit of the spectra in the spectral regions of the H_β and He I at 4921.9 Å lines. Once the best fit is reached, we estimated again the abundance of helium by fitting each of the available lines. The results are reported in Tables 4 and 5, where we show the photometric values considered as input parameters, the ones resulting from our best fit, and the mean abundance of He, respectively.

The photometric and spectroscopic values of the temperatures and gravities are in a good agreement, within the errors, except for A5 and A48. It is interesting to note that the obtained $T_{\rm eff}^{\rm spec}$ (K) and log$g^{\rm spec}$ values are also in fair agreement, within the uncertainties, with the ones found from non-rotating models.

The fitting procedure disclosed that, for some stars such as A5, A17, and A23, the projected rotation velocity obtained from spectroscopy moves away from the input values, typically decreasing their values. The highest *v*sini are found for the stars A5 and A10, as also evident from Figure 7. In fact, when the stellar rotation is taken into account, the quality of the fit improves and the best fit is obtained for nearly all the available He lines.

Figure 10 shows the helium abundance of each star. Black filled and red empty circles represent, respectively, the mean helium abundance with or without considering the stellar rotation. The measured mean abundances determined considering the rotation are systematically higher than those calculated without rotation. This result agrees with the expectations from the theory discussed in Section 3.1. We note that A4 is an exception, with the mean value obtained considering the rotation slightly lower than the one determined without rotation. For this star is not possible to fit all spectral lines considering the stellar rotation. For this reason, we suggest that this source is not a rotating star, in agreement with Lennon et al. (2003).

Even if the resolution of the data and the uncertainties of the results require caution, we find that the rotating framework seems to suggest higher helium abundances than the values found using non-rotating models. The mean $\langle \epsilon\,(\mathrm{He})\rangle_{\rm rot} = 11.00 \pm 0.05$ can be compared with the value obtained for the non-rotating one, $\langle \epsilon\,(\mathrm{He})\rangle = 10.93 \pm 0.05$.

Unfortunately, we could not reach conclusive results to determine the preferred scenario about rotation, nevertheless this work provides two possible evaluations of the helium abundances for the two cases, one for fully non-rotating massive stars and one for rotating stars.

4.4. NLTE Effect

Conditions of NLTE could play a role on the estimation of the He abundance because they affect both line cores and wings and therefore the equivalent widths of the He lines. (Schneider et al. 2018; Przybilla 2005). For this reason, in this section we briefly discuss the NLTE effect.

Schneider et al. (2018) analyzed He I lines in the optical range of several B-type main-sequence stars, studying also the isotopic shift of the ^{4}He due to the presence of the ^{3}He with the NLTE approach. From high-resolution spectra, they found the strongest departure from the LTE approach for the He I 5875.6 Å line. They compared the He abundance of the B type with $20{,}000 < T_{\rm eff} < 30{,}000$ K analyzed the NLTE approach with that found in the literature with the LTE approach (see their Table 4). This table shows that the values determined with the LTE are roughly in agreement, within the errors, with those

Table 4
Input (Photometric) and Output (Spectroscopic) Parameters Obtained from Our Analysis Considering the Stellar Rotation Velocity. Errors in Spectroscopic Parameters are Listed for Each Target

Star	$T_{\rm eff}^{\rm phot}$(K)	$\sigma(T_{\rm eff}^{\rm phot})$(K)	$\log g^{\rm phot}$	$\sigma(\log g^{\rm phot})$	$v \sin i^{\rm input}$(km s^{-1})	$T_{\rm eff}^{\rm spec}$ (K)	$\sigma(T_{\rm eff}^{\rm spec})$(K)	$\log g^{\rm spec}$	$\sigma(\log g^{\rm spec})$	$v \sin i^{\rm output}$(km s^{-1})
A4	16800	1000	3.0	0.5	100	17000	1000	2.9	0.1	100
A5	16000	1000	3.8	0.5	350	21400	3000	3.5	0.2	250
A10	18500	1000	3.2	0.5	250	20500	1000	3.7	0.1	200
A17	20000	1000	3.3	0.5	180	21700	1000	3.6	0.1	100
A21	19000	1000	3.3	0.5	170	21000	1000	3.6	0.2	150
A23	22000	1000	3.5	0.5	230	21600	2000	3.6	0.2	100
A24	20500	1000	3.4	0.5	330	21700	1500	3.9	0.3	150
A34	17800	1000	3.8	0.5	300	20500	1500	3.8	0.2	150
A40	16500	1000	2.9	0.5	100	17500	500	3.1	0.1	100
A48	18000	1000	3.1	0.5	150	22000	1500	3.1	0.3	150

Table 5
Mean Values, Within 1σ of the He Abundance, for Each Star of the Sample Obtained Considering Stellar Rotation

Star	$\langle\epsilon\,(\rm He)\rangle_{\rm rot}$	σ	$Y_{\rm rot}$	$\sigma\,(Y)$
A4	10.90	0.3	0.24	0.25
A5	11.02	0.03	0.29	0.03
A10	10.96	0.04	0.27	0.04
A17	10.98	0.03	0.27	0.03
A21	10.98	0.08	0.28	0.07
A23	10.98	0.10	0.28	0.10
A24	11.08	0.20	0.32	0.20
A34	11.11	0.10	0.34	0.10
A40	11.02	0.10	0.30	0.09
A48	10.88	0.21	0.23	0.17

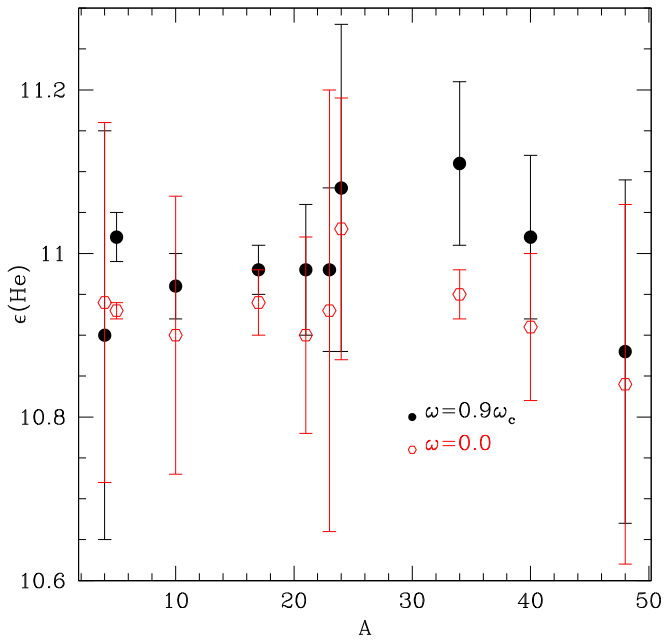

Figure 10. Mean value of the He abundance for each target considering $\omega = 0.9\omega_c$ (black points) and $\omega = 0.0$ (red points). Error bars are also shown.

found with the NLTE approach, and the systematic uncertainties on $\log(n_{\rm he})$ evaluated are reported of the order of ± 0.1.

Recalling that the resolution of our data is about 2000, while Schneider et al. (2018) used spectra with a spectral resolution between 18,000 and 60,000, we clarify that the NLTE analysis is not possible here and it is beyond the limit of the feasibility with the resolution of the MUSE spectra. Moreover, the uncertainties in the He abundances derived in this work are larger than the indetermination due to the LTE/NLTE differences evaluated by Schneider et al. (2018). Thus, the NLTE approach is not adopted in our analysis.

Finally, the diffusive effect process is not taken into account in our analysis on the He abundance because the hot massive stars are characterized by a strong mass loss and rotational mixing, which tend to limit or completely erase the effect of diffusion (Salaris & Cassisi 2017).

5. Discussion

5.1. Cluster Age

The photometric results of the bright region of the CMD of NGC 330 (see Section 3) suggest once more that the blue and red groups of supergiants, clearly identified since early studies, are due to core He-burning stars (e.g., Stothers & Chin 1992; Brocato & Castellani 1993). In this work, we also suggest that at least two isochrones are needed to reproduce the position of these stars in the CMD. In the non-rotation case, the separation in age we find between the two isochrones is ≈12 Myr. This partially supports the result obtained by Li et al. (2017) for four clusters in the MCs (including NGC 330). In fact, Li et al. have found that a spread of 35–50 Myr has to be considered to explain the extended main-sequence turnoffs in these clusters, while the rotation alone could not account for this observational evidence. On the other hand, Bodensteiner et al. (2020) appear to support a smaller spread of the order of 5 Myr.

We hence support the suggestion by Li et al. (2017) using other observables, i.e., the core He-burning stars. We point out that the best fit of the two isochrones (at 18 and 30 Myr) were found on the basis of differential magnitudes of very bright and well-measured stars. This secures that we are dealing with differential magnitude uncertainties that are very small (≈0.02 mag).

Uncertainties on absolute calibrations related to distance modulus, reddening, calibrations, and theoretical assumptions are not expected to severely affect the difference in age between the isochrones fitting the data, while they may change the absolute age evaluations.

A weakness of this argument is the fact that blue supergiants in the observed CMD are few and far from any robust statistical sample, in comparison to the large number of main-sequence stars. This is consequence of the evolutionary timescales of the core He-burning, which are a factor of ≈10 times shorter than the ones of the core H-burning evolutionary phase lifetimes.

Table 6
Mean Helium Abundance of NGC 330 (see the text)

	$\langle\epsilon\,(\mathrm{He})\rangle$	$\sigma_{\langle\epsilon\,(\mathrm{He})\rangle}$	$\langle Y\rangle$	$\sigma_{\langle Y\rangle}$
MUSE sample	10.93	0.05	0.25	0.02
Other works	10.79	0.13	0.20	0.05
Entire sample	10.88	0.10	0.23	0.04
∼18 Myr stars	10.84	0.13	0.22	0.05
∼30 Myr stars	10.91	0.08	0.25	0.03

Nevertheless, NGC 330 is one of the youngest and most massive star clusters in the local universe and, for this reason, it remains a fundamental ensemble of stars to be considered in studying young stellar populations.

It is interesting to highlight here that the mass of the stars in the core He-burning phase obtained from the data of the two best-fit isochrones are $9.2 \pm 0.1 M_{\odot}$ and $12.5 \pm 0.2\,M_{\odot}$ (Bressan et al. 2012; Marigo et al. 2017). Since the ratio of their evolutionary time during this phase is ≈6 (estimated from the tracks consistent with the isochrones; Bressan et al. 2012), this is in fair agreement with the small number of stars observed at younger age (4:1 in our—homogeneous but not complete—sample).

Finally, we recall a further point related to stellar rotation. As we show in Figure 5, isochrones computed with stellar models that take into account rotation affect the determination of the age of the stellar populations of NGC 330. In fact, in Section 3.1 we show that the CMD can be explained by one nearly coeval stellar population composed by a mixture of rotating and non-rotating stars.

5.2. He Abundance and Age

The presence of an age spread in the stellar population of NGC 330 leads us to investigate the existence of possible star-to-star difference in He abundance. Using the results obtained in Section 4, we now investigate possible relationships between He abundance and general properties of the cluster.

We evaluated the mean He abundance of NGC 330 as obtained considering our homogeneous set of MUSE data (we call these stars the MUSE sample in Table 6), i.e., $\epsilon\,(\mathrm{He})_{\mathrm{MUSE\ sample}} = 10.93 \pm 0.05$ (see also Figure 11). Moreover, considering the sample of stars analyzed by Lennon et al. (2003), namely A1, A2, A4, B4, B22, B32, and B37, and the star B30 studied by Korn et al. (2000), we obtain an average of $\epsilon(\mathrm{He})_{\mathrm{other\ works}} = 10.79 \pm 0.13$. Considering both He abundance results of our MUSE sample and of other works, the global value we obtain from the entire sample of stars with available He abundances is $\epsilon(\mathrm{He})_{\mathrm{entire\ sample}} = 10.88 \pm 0.10$ (see Table 6). In this calculation we have considered as helium abundance of the A4 star, which was obtained with MUSE sample. Therefore we can conclude that the average value of the He abundance of NGC 330 obtained with our (homogeneous) sample is consistent, within the uncertainties, with that found considering the entire—not homogeneous—sample.

We now investigate possible relationships between He abundance and stellar age. To this purpose, we tried to assign to each star of the MUSE sample the age of the nearest isochrone according to their CMD location. Unfortunately, the differences in color between the isochrones are too small to make a safe separation among stars located near the blue (older) or the red (younger) isochrones (see Figure 4). We

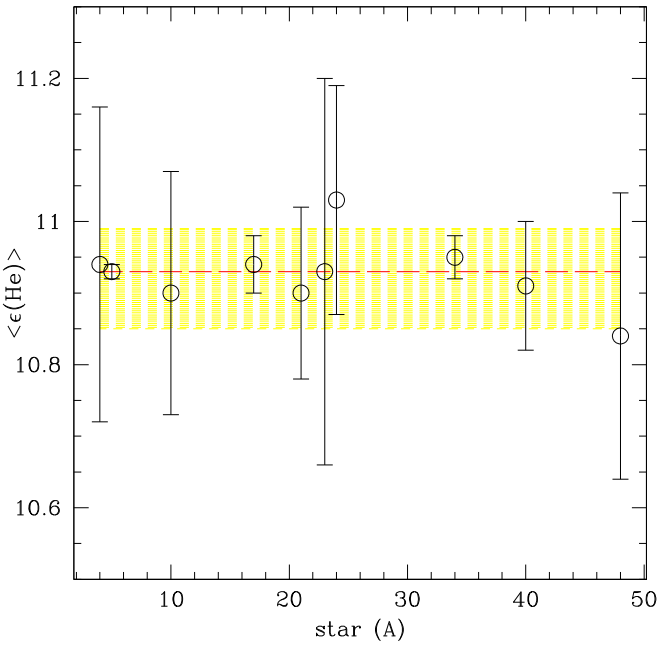

Figure 11. Mean value of the logarithmic He abundance for each target. Error bars are also shown. The red dashed line represents the average of these values, while the yellow shadow region shows the $\pm 1\sigma$ level.

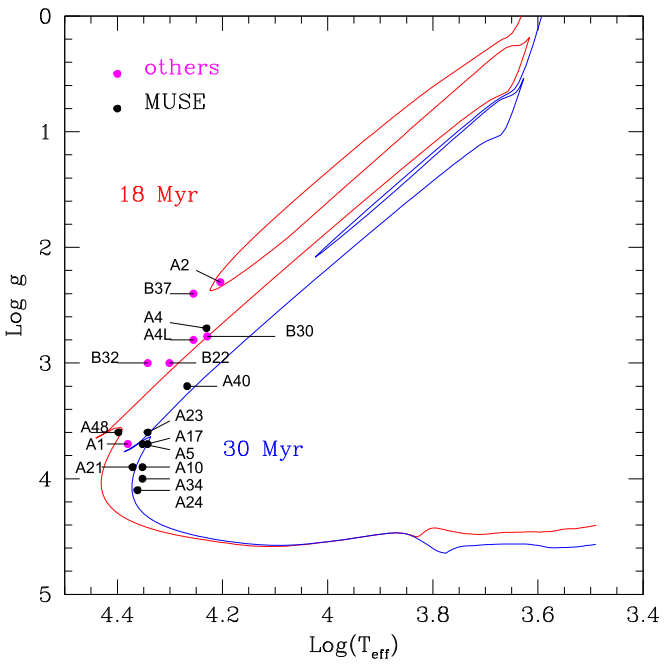

Figure 12. $\log T_{\mathrm{eff}} - \log g$ diagram for the stars analyzed spectroscopically by us with MUSE (black dots) and by other authors (magenta dots). The $Z = 0.002$ PARSEC isochrones of 18 and 30 Myr are also reported with red and blue solid lines, respectively. We also report the name of the stars. We show the $\log T_{\mathrm{eff}}$ and $\log g$ of A4 determined by us (A4) and by Lennon et al. (2003; A4L).

therefore considered the $\log T_{\mathrm{eff}} - \log g$ diagram for both the MUSE sample and the stars analyzed in other works.

The $\log T_{\mathrm{eff}} - \log g$ diagram of the entire sample of NGC 330 stars with He abundance determination is presented in Figure 12.

First, this plot confirms our previous findings that the stars of NGC 330 seem to show age differences/spread of ∼12 Myr. Then, if we arbitrarily assume from the $\log T_{\mathrm{eff}} - \log g$

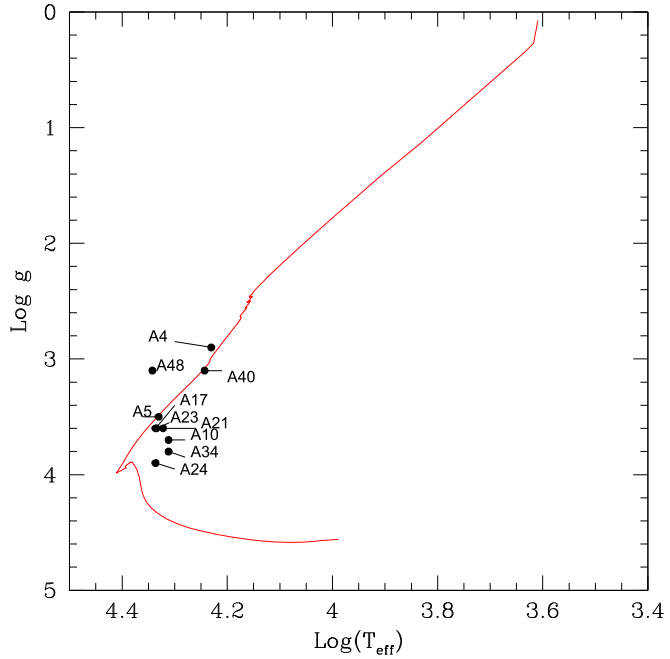

Figure 13. log $T_{\rm eff}$ − log g diagram for the stars analyzed spectroscopically by us with MUSE (black dots) considering stellar rotation. The $Z = 0.002$ SYCLIST isochrones of 30 Myr and $\omega = 0.9\omega_c$ (Georgy et al. 2014) is reported with the red solid line. We report also the names of the stars.

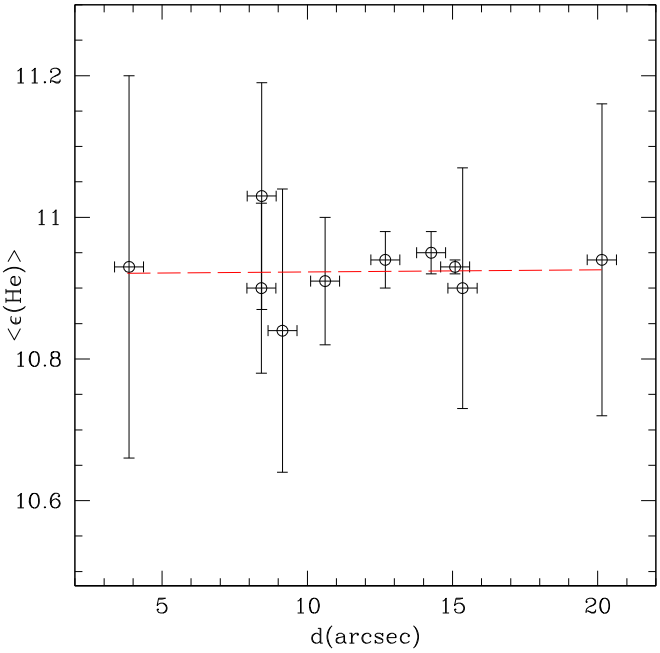

Figure 14. He abundance versus distance from the center of NGC 330 for our MUSE sample. The dashed line represents the linear best fit to the data. The effective radius of NGC 330 is at 20″.

diagram an age of 18 Myr for the stars A2, A4, A48, B22, B30, B32, and B37, and an age of 30 Myr for the stars A1, A5, A10, A17, A21, A23, A24, A34, and A40, the mean He abundance for each group of stars is $\langle \epsilon\,(\mathrm{He})\rangle_{18\ \mathrm{Myr}} = 10.85 \pm 0.13$ and $\langle \epsilon\,(\mathrm{He})\rangle_{30\ \mathrm{Myr}} \approx 10.92 \pm 0.07$, respectively (see Table 3). We hence find that, within the errors, the resulting He abundances of the two groups of stars separated in age do not show relevant differences.

If the rotational scenario is taken into account, the log $T_{\rm eff}$ − log g diagram changes (see Figure 13), first because the fits of the spectra provide different values of $T_{\rm eff}$ and log g when the rotation of the star is considered and second because the isochrone obtained by rotating stellar model has a different pattern from a non-rotating isochrone.

The rotating isochrone of 30 Myr, which reproduces the CMD of NGC 330 in Figure 5 and fails to match the position in the log $T_{\rm eff}$ − log g diagram of several stars (A24, A34, A10, A21, A23, A17, and A48). On the contrary, the bright stars (A4, A5, and A40) appear to be located along the pattern of this isochrone. Thus, this comparison suggests once more that a scenario in which the massive stars in NGC 330 could have the same age but experience a different rotation velocity cannot be excluded. In this plot we have not considered the sources analyzed by Lennon et al. (2003) and Korn et al. (2000) because the authors considered their stars as non-rotating.

If the hypothesis of coeval populations is considered, we find that the mean helium abundance within 1σ of the only rotating stellar population is $\sim$10.98 ($Y \sim 0.28$), slightly higher than the mean value obtained for the non-rotating stars ($\sim$10.93, $Y \sim 0.25$). As already mentioned in Section 2, the region covered by our MUSE observations is comparable with the annulus "A" of Robertson (1974) and our targets are located within the effective radius of the cluster ($R_{\rm eff} = 20''$; Portegies Zwart et al. 2010). We can therefore investigate in this internal cluster region the behavior of the stellar He abundance with the distance from the center.

In Figure 14, we present our ϵ(He) values obtained using homogeneous MUSE data as a function of the distance of each star from the cluster center (d). The center of the cluster was defined according to the definition of Evans et al. (2006), i.e., $\alpha(J2000) = 00^{\rm h}56^{\rm m}18\overset{\rm s}{.}8$ and $\delta(J2000) = -72°56'18\overset{''}{.}8$. The result of our investigation clearly points out that there is no correlation between the distance of the stars from the center of the cluster and their He abundances. This can be also quantified by a Kendalls' rank correlation. For this test we found a significance of about 0.71 for the ϵ(He) distance and 0.70 for the Y-distance correlations. This means that there is no apparent correlation between the two samples of data (see Figure 14).

6. Conclusion

We have presented an homogeneous analysis of photometric and spectroscopic data of the SMC young cluster NGC 330. The results can be summarized as follows.

1. We have found a possible difference in the age of the stars within NGC 330 with a spread/separation of the order of ≈12 Myr. This evidence has been derived also on the basis of the photometry of core He-burning stars. However, further observational studies are required to investigate if the brightest (youngest?) stars are binaries or not.
2. We cannot exclude that the age spread is reduced or disappears, if stellar rotation is considered.
3. We have measured for the first time the He abundance of 10 stars placed in the center of NGC 330 (e.g., $r_{\rm star} \leqslant R_{\rm eff}$). We have found a mean value of $\langle \epsilon\,(\mathrm{He})\rangle = 10.93 \pm 0.05$ for our targets homogeneously analyzed with MUSE at the VLT.

4. Considering also the stars studied in the past in this cluster, we have found a mean global helium abundance of $\langle \epsilon\,(\mathrm{He})\rangle = 10.88 \pm 0.10$, consistent with our value homogeneously derived.
5. We evaluated the effect of rotation on the He abundance by fitting our spectra assuming the v sin i value for which the fit is reached. In this case a mean global helium abundance of $\langle \epsilon\,(\mathrm{He})\rangle_{\mathrm{rot}} = 11.00 \pm 0.05$ is found.
6. Finally, for the main-sequence B stars with $r_{\mathrm{star}} \leqslant R_{\mathrm{eff}}$, we have not found a possible correlation of the stellar helium abundance with the distance from the cluster center.

The results reported in this work need more robust confirmation and we are working to increase the statistics and to minimize uncertainties. In particular, we intend to obtain a larger sample of spectra of NGC330 B stars to increase the number of He abundance measurements of the 18 Myr stellar population. Moreover, we will also derive the He abundance for all the core He-burning stars of both populations. Nevertheless, the results obtained in this paper show that MUSE at the VLT is an extremely powerful instrument able to investigate both photometric and spectroscopic properties of stellar populations in young stellar clusters.

This work has made use of the VALD database, operated at Uppsala University, the Institute of Astronomy RAS in Moscow, and the University of Vienna. K.B. thanks the Osservatorio Astronomico di Roma for the hospitality during the preparation of the paper. We thank the anonymous referee for the valuable comments and suggestions that improved the quality of the publication. We thank Antonio Sollima for his precious feedback.

Software: daophot (Stetson 1987), PARSEC (Bressan et al. 2012; Marigo et al. 2017), SYCLIST (Georgy et al. 2014), molecfit (Smette et al. 2015; Kausch et al. 2015), SME (Valenti & Piskunov 2012), ATLAS12 (Kurucz 1979).

ORCID iDs

R. Carini https://orcid.org/0000-0003-1604-2064
K. Biazzo https://orcid.org/0000-0002-1892-2180
E. Brocato https://orcid.org/0000-0001-7988-8177
L. Pulone https://orcid.org/0000-0002-5285-998X

References

Arp, B. H. 1959, AJ, 64, 254
Asplund, M., Gravesse, N., Sauval, A. J., & Scott, P. 2009, ARA&A, 47, 481
Bacon, R., Accardo, M., Adjali, L., et al. 2010, Proc. SPIE, 7735, 773508
Bastian, N., & de Mink, S. E. 2009, MNRAS, 398, L11
Bastian, N., Lamers, H. J. G. L. M., de Mink, S. E., et al. 2013, MNRAS, 436, 2398
Bodensteiner, J., Sana, H., Mahy, L., et al. 2020, A&A, 634, A51
Brandt, T. D., & Huang, C. X. 2015, ApJ, 807, 25
Bressan, A., Marigo, P., Girardi, L., et al. 2012, MNRAS, 427, 127
Brocato, E., & Castellani, V. 1993, ApJ, 410, 99
Brunish, W. M., Gallagher, J. S., & Truran, J. W. 1986, AJ, 91, 598
Caloi, V., Cassatella, A., Castellani, V., & Walker, A. 1993, A&A, 271, 109
Carretta, E. 2015, ApJ, 810, 148
Carretta, E., Bragaglia, A., Gratton, R. G., et al. 2009, A&A, 505, 117
Carretta, E., Bragaglia, A., Lucatello, S., et al. 2018, A&A, 615, A17
Castelli, F., & Kurucz, R. L. 2003, in Proc. IAU Symp. 210, Modeling of Stellar Atmospheres, ed. N. Piskunov, W. W. Weiss, & D. F. Gray (San Fransisco, CA: ASP), A20
Chantereau, W., Salaris, M., Bastian, N., & Martocchia, S. 2019, MNRAS, 484, 5236
Chiosi, C., Vallenari, A., Bressan, A., Deng, L., & Ortolani, S. 1995, A&A, 293, 710
D'Antona, F., & Caloi, V. 2004, ApJ, 611, 871
D'Antona, F., Di Criscienzo, M., Decressin, T., et al. 2015, MNRAS, 453, 2637
Decressin, T., Charbonnel, C., & Meynet, G. 2007, A&A, 475, 859
D'Ercole, A., D'Antona, F., & Vesperini, E. 2016, MNRAS, 461, 4088
D'Ercole, A., Vesperini, E., D'Antona, F., McMillan, S., & Recchi, S. 2008, MNRAS, 391, 825
Evans, C. J., Lennon, D. J., Smartt, S. J., & Trundle, C. 2006, A&A, 456, 623
Feast, M. W. 1991, in Proc. IAU Symp. 148, The Magellanic Clouds, ed. R. Haynes & D. Milne (Dordrecht: Kluwer), 1
Georgy, C., Granada, A., Ekström, S., et al. 2014, A&A, 566, A21
Gieles, M., Charbonnel, C., Krause, M. G. H., et al. 2018, MNRAS, 478, 2461
Girardi, L., Rubele, S., & Kerber, L. 2009, MNRAS, 394, L74
Glatt, K., Grebel, E. K., & Sabbi, E. 2008, AJ, 136, 1703
Goudfrooij, P., Girardi, L., Kozhurina-Platais, V., et al. 2014, ApJ, 797, 35
Gratton, R., Bragaglia, A., Carretta, E., et al. 2019, A&ARv, 27, 8
Gratton, R. G., Carretta, E., & Bragaglia, A. 2012, A&ARv, 20, 50G
Grebel, E. K., & Richtler, T. 1992, A&A, 253, 359
Grebel, E. K., Roberts, W. J., & Brandner, W. 1996, A&A, 311, 470
Hill, V. 1999, A&A, 345, 430
Hunter, I., Lennon, D. J., Dufton, P. L., et al. 2011, A&A, 530, C1
Kausch, W., Noll, S., Smette, A., et al. 2015, A&A, 576, A78
Keller, S. C., & Bessell, M. S. 1998, A&A, 340, 397
Keller, S. C., Bessell, M. S., & Da Costa, G. S. 2000, AJ, 119, 1748
Keller, S. C., Wood, P. R., & Bessell, M. S. 1999, A&AS, 134, 489
Kelz, A., Kamann, S., Urrutia, T., Weilbacher, P., & Bacon, R. 2016, in ASP Conf. Ser. 507, Multi-object Spectroscopy in the Next Decade: Big Questions, Large Surveys, and Wide Fields, ed. I. Skillen, M. Balcells, & S. Trager (San Francisco: ASP), 323
Korn, A. J., Becker, S. R., Gummersbach, C. A., & Wolf, B. 2000, A&A, 353, 655
Kurucz, R. L. 1979, ApJS, 40, 1
Kurucz, R. L. 2013, ATLAS12: Opacity sampling model atmosphere program, Astrophysics Source Code Library, ascl:1303.024
Lagioia, E. P., Milone, A. P., Marino, A. F., Cordoni, G., & Tailo, M. 2019a, AJ, 158, 202
Lagioia, E. P., Milone, A. P., Marino, A. F., & Dotter, A. 2019b, ApJ, 871, 140
Landolt, A. U. 1992, AJ, 104, 340
Langer, N., & Maeder, A. 1995, A&A, 295, 685
Lennon, D. J., Dufton, P. L., & Crowley, C. 2003, A&A, 398, 455
Lennon, D. J., Dufton, P. L., Mazzali, P. A., Pasian, F., & Marconi, G. 1996, A&A, 314, 243
Li, C., de Grijs, R., Deng, L., & Milone, A. P. 2017, ApJ, 844, 119
Mackey, A. D., & Broby Nielsen, P. 2007, MNRAS, 379, 151
Mackey, A. D., & Gilmore, G. F. 2003, MNRAS, 338, 120
Maeder, A., Grebel, E. K., & Mermilliod, J.-C. 1999, A&A, 346, 459
Maeder, A., & Meynet, G. 2000, ARA&A, 38, 143
Marigo, P., Girardi, L., Bressan, A., et al. 2017, ApJ, 835, 77
Marino, A. F., Milone, A. P., Przybilla, N., et al. 2014, MNRAS, 437, 1609
Marino, A. F., Przybilla, N., Milone, A. P., et al. 2018, AJ, 156, 116
Martayan, C., Floquet, M., Hubert, A. M., et al. 2007a, A&A, 472, 577
Martayan, C., Frémat, Y., Hubert, A.-M., et al. 2007b, A&A, 462, 683
Martocchia, S., Bastian, N., Usher, C., et al. 2017, MNRAS, 468, 3150
Mazzali, P. A., Lennon, D. J., Pasian, F., et al. 1996, A&A, 316, 173
McLaughlin, D. E., & van der Marel, R. P. 2005, ApJS, 161, 304
Meliani, M. T., Barbuy, B., & Perrin, M.-N. 1995, A&A, 300, 349
Meynet, G., & Maeder, A. 2000, A&A, 361, 101
Milone, A. P., Bedin, L. R., Piotto, G., et al. 2015, MNRAS, 450, 3750
Milone, A. P., Bedin, L. R., Piotto, G., & Anderson, J. 2009, A&A, 497, 755
Milone, A. P., Marino, A. F., D'Antona, F., et al. 2016, MNRAS, 458, 4368
Milone, A. P., Marino, A. F., D'Antona, F., et al. 2017, MNRAS, 465, 4363
Milone, A. P., Marino, A. F., Di Criscienzo, M., et al. 2018, MNRAS, 477, 2640
Mucciarelli, A., Dalessandro, E., Ferraro, F. R., Origlia, L., & Lanzoni, B. 2014, ApJL, 793, L6
Pasquini, L., Mauas, P., Kaufl, H. U., & Cacciari, C. 2011, A&A, 531, 35
Piotto, G. 2008, MmSAI, 79, 334
Piotto, G. 2010, PKAS, 25, 91
Piotto, G., Bedin, L. R., Anderson, J., et al. 2007, ApJL, 661, L53
Piskunov, N., & Valenti, J. A. 2017, A&A, 597, A16
Piskunov, N. E., Kupka, F., Ryabchikova, T. A., Weiss, W. W., & Jeffery, C. S. 1995, A&AS, 112, 525
Portegies Zwart, S. F., McMillan, S. L. W., & Gieles, M. 2010, ARA&A, 48, 431
Press, W. H., Teukolsky, S. A., Vetterling, W. T., & Flannery, B. P. 1992, Numerical Recipes (Cambridge: Cambridge Univ. Press)

Press, W. H., Teukolsky, S. A., Vetterling, W. T., & Flannery, B. P. 2002, Numerical Recipes in C++: the Art of Scientific Computing (Cambridge: Cambridge Univ. Press)
Przybilla, N. 2005, A&A, 443, 293
Reitermann, A., Baschek, B., Stahl, O., & Wolf, B. 1990, A&A, 234, 109
Richtler, T., & Nelles, B. 1983, A&A, 119, 75
Robertson, J. W. 1974, A&AS, 15, 261
Salaris, M., & Cassisi, S. 2017, RSOS, 4, 170192
Schaller, G., Schaerer, D., Meynet, G., & Maeder, A. 1992, A&AS, 96, 269
Schneider, D., Irrgang, A., Heber, U., Nieva, M. F., & Przybilla, N. 2018, A&A, 618, A86
Sirianni, M., Nota, A., De Marchi, G., Leitherer, C., & Clampin, M. 2002, ApJ, 579, 275
Smette, A., Sana, H., Noll, S., et al. 2015, A&A, 576, A77
Spite, F., Spite, M., & Richtler, T. 1991, A&A, 252, 557
Stetson, P. B. 1987, PASP, 99, 191
Stothers, R. B., & Chin, C.-W. 1992, ApJ, 390, 136
Tanabé, T., Motohara, K., Tateuchi, K., et al. 2013, PASJ, 65, 55
Udalski, A., Soszyński, I., Szymański, M. K., et al. 2008, AcA, 58, 329
Udalski, A., Szymanski, M., Kubiak, M., et al. 1998, AcA, 48, 147
Valenti, J. A., & Piskunov, N. 1996, A&AS, 118, 595
Valenti, J. A., & Piskunov, N. 2012, SME: Spectroscopy Made Easy, Astrophysics Source Code Library, ascl:1202.013
W. Marquardt, D. 1963, J. Soc. Ind. Appl. Math., 11, 431
Weilbacher, P. M., Streicher, O., Urrutia, T., et al. 2014, in ASP Conf. Ser. 485, Astronomical Data Analysis Software and Systems XXIII, ed. N. Manset & P. Forshay (San Francisco, CA: ASP), 451